IMMUNOLOGY

Rebalancing viral and immune damage versus repair prevents death from lethal influenza infection

Hiroshi Ichise*, Emily Speranza, Federica La Russa, Tibor Z. Veres, Colin J. Chu, Anita Gola, Beatrice H. Clark, Ronald N. Germain*

INTRODUCTION: Pulmonary viral infections account for substantial numbers of deaths annually and many more during pandemics such as influenza in 1918 and severe acute respiratory syndrome coronavirus 2 (COVID-19) in 2020. Most studies ascribe loss of pulmonary function to a combination of viral destruction of infected cells and tissue damage from excessive innate inflammatory responses, and thus, inhibition of such innate activity in infected individuals has been the focus of much research.

RATIONALE: Given the strong evidence that innate immunity makes a major contribution to lethality in influenza, we screened a broad array of agents to identify those capable of preventing lethal influenza in a mouse model. The experimental model was designed to cause death within a narrow time window (8 to 10 days) in all infected animals so that survival of even a few animals in a group given any single treatment would constitute a consequential signal. If such signs of activity were found and with the treatments acting on different innate immune elements, a limited number of combinatorial therapies could be examined for additive synergy.

RESULTS: Apart from neutrophil depletion at one day after infection, none of 50 different therapies led to survival of infected animals. This was despite the use of some treatments focused on one inflammatory mediator, such as interleukin-6, and others that blocked signaling pathways affecting multiple downstream innate responses. These data suggested a tipping point model in which early damage from the combination of viral pathogenicity and inflammation led to delayed, but inevitable, death and where inhibition of further innate inflammatory responses could not rescue pulmonary function. Prior data indicated that repair processes begin almost immediately upon infection. This led us to hypothesize that failure of repair processes to counterbalance early and ongoing damage was insufficient to sustain pulmonary function in the absence of extrinsic gas exchange support (e.g., mechanical ventilation). We designed late postinfection treatments that combined partial limitation of viral spread using Tamiflu with either an anti–interferon-α/β receptor (αIFNAR) treatment, to reverse type I interferon (IFN) suppression of alveolar type 1 (AT1) pneumocyte replacement, or depletion of cytotoxic CD8+ effector T cells, to prevent killing of infected pneumocytes late in disease. Despite starting treatment late after infection, both combinations, of Tamiflu and αIFNAR or Tamiflu and anti-CD8 (αCD8), led to a substantial increase in animal survival beyond antiviral therapy alone.

CONCLUSION: This study clarified why anti-inflammatory therapies other than high-dose steroids have had limited impact on the course of advanced pulmonary viral infections. Hosts with severe disease late in the infectious cycle are likely to be past the point at which arresting the damage caused by innate immune cells is enough to prevent loss of essential pulmonary function; rather, it is the failure to repair tissue damage or the additional damaging effect of adaptive, T cell–mediated, immunity that are critical at this time. This view is consistent with the prolonged time on ventilators often required for recovery of patients with severe disease and low blood oxygen saturation. Our results also indicate that antiviral drugs can be beneficial well after symptoms begin if combined with treatments that encourage repair directly or that ameliorate subsequent adaptive immune damage. □

*Corresponding author. Email: rgermain@niaid.nih.gov (R.N.G.); hiroshi.ichise@nih.gov (H.I.) Cite this article as H. Ichise *et al.*, *Science* 390, eadr4635 (2025). DOI: 10.1126/science.adr4635

Combining antiviral drug therapy with inhibition of type I IFN signaling or depletion of CD8+ effector T cells improves survival from influenza infection. In severe influenza, early innate immune and viral damage reduces lung function below a tipping point, beyond which limiting further damage alone cannot restore function. CD8+ T cells further exacerbate damage by eliminating infected epithelial cells, despite repair induction. Combining antiviral therapy with type I IFN blockade or CD8+ T cell depletion enhances survival by shifting the balance toward repair over damage, maintaining pulmonary function. dpi, days postinfection; pSTAT, phospho-signal transducer and activator of transcription; IAV, influenza A virus. [Figure created with BioRender.com]
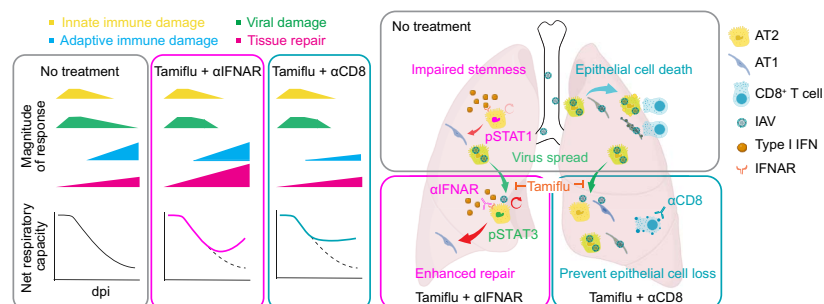
IMMUNOLOGY

Rebalancing viral and immune damage versus repair prevents death from lethal influenza infection

Hiroshi Ichise[1]*, Emily Speranza[2], Federica La Russa[1], Tibor Z. Veres[1], Colin J. Chu[3], Anita Gola[1], Beatrice H. Clark[1], Ronald N. Germain[1,4]*

Maintaining tissue function while eliminating infected cells is fundamental, and inflammatory damage plays a major contribution to lethality after lung infection. We tested 50 immunomodulatory regimes to determine their ability to protect mice from lethal infection. Only neutrophil depletion soon after infection prevented death from influenza. This result suggests that the infected host passed an early tipping point after which limiting innate damage alone could not rescue lung function. We investigated treatments that could have efficacy when administered later in infection. We found that partial limitation of viral spread together with enhancement of epithelial repair, by interferon blockade or limiting CD8+ T cell–mediated killing of epithelial cells, reduced lethality. This finding highlights the importance of rebalancing repair and damage processes in the survival of pulmonary infections.

Despite wide availability of antiviral drugs and vaccines, seasonal influenza can be life-threatening and lead to pneumonia and acute respiratory distress syndrome (ARDS) (*1*). Beyond this typical seasonal threat, influenza has caused multiple worldwide pandemics in the past 100 years (*2*, *3*). Fatal influenza is associated with widespread pneumonia (*4*), and dysregulated innate immunity is a major cause of the tissue damage in such infections (*5–8*). Preclinical studies have identified type I interferon (IFN) (*6*), neutrophils (*5*, *9*), and CCR2+ monocyte-derived dendritic cells (*8*) as major contributors to this damage. Excessive innate immune responses are also a hallmark of severe acute respiratory syndrome (SARS), Middle East respiratory syndrome (MERS), and COVID-19 (*10–13*). Anti-inflammatory treatments have been extensively studied in attempts to ameliorate severe influenza (*14*), but antiviral treatment remains the only option recommended by the Centers for Disease Control and Prevention (*15*). For COVID-19, high-dose steroids have been found to be moderately effective (*16*), whereas immunosuppressive agents with greater selectivity have modest effects when used late in the course of infection (*17*).

Temporal understanding of pathogenesis is important for developing clinical interventions in diverse disease states. An early fatal gene signature associated with a neutrophil-mediated inflammatory feed forward circuit is seen at very early stages of influenza infection, and acute depletion of neutrophils improves survival (*5*). Other research has shown that while type I IFNs contribute to rapid antiviral responses that limit pathogen spread, the timing of production of this cytokine is critical to preventing a pathogenic innate immune response

in severe acute respiratory syndrome coronavirus (SARS-CoV) infection (*18*). This suggests that the limited treatment success of agents that inhibit the innate immune response in viral pneumonias might be due to their late administration. One of the earliest gene expression signatures accompanying the intense innate inflammatory response to severe influenza infection is that of tissue repair (*5*). Tissue repair is essential to compensate for damage caused by viral cytopathic effects and the activity of immune cells. The tissue disruption caused by the innate inflammatory response may have already passed a tipping point that does not allow return to a lung physiological state solely through further limitation of damage from such pathways. In this study, we examined this tipping point model in the context of a balance between tissue damage and repair, seeking to identify potential protective interventions.

Results

An oropharyngeal lethal influenza infection causes severe lung pathology

To develop a lethal influenza infection model that causes severe lung pathology, we used the oropharyngeal route and titrated the dose of influenza A/Puerto Rico/8/34 (PR8) used for infection (fig. S1, A and B). We identified the minimum viral load that produced a uniformly lethal outcome and performed a time-resolved multiplex immunological profiling of the lungs, blood, bone marrow, and lung-draining lymph nodes of the infected animals (Fig. 1A). After infection, mice showed ruffled fur, hunching, and strained breathing starting around 3 days postinfection (dpi). Viral RNA in the lung peaked at 2 dpi, and animals lost weight starting at 4 dpi, succumbing to infection between 8 and 10 dpi (Fig. 1B and fig. S1, C and D). RNA sequencing (RNA-seq) was conducted on the whole lung at 4, 6, and 8 dpi. Reads associated with viral RNA matched with the quantitative polymerase chain reaction (qPCR) results and showed an increase at 4 dpi that was sustained to 6 dpi. By 8 dpi, when animals were in a preterminal condition, the viral RNA began to decline (fig. S1E). Transcriptional analysis showed early and strong signals associated with interferon signaling and inflammation by 4 dpi, followed by T cell responses at 6 dpi and a burst in cell proliferation at 8 dpi, suggesting ongoing repair processes (Fig. 1, C and D). Cell type deconvolution of the transcriptional data showed early loss of alveolar type 2 (AT2) cells by 4 dpi, with infiltration of neutrophils and macrophage-like populations at 6 dpi (fig. S1F). These changes were confirmed by flow cytometric analysis showing sequential recruitment of neutrophil, myeloid, and T cell populations to the lung (Fig. 1E and fig. S2). Additional flow cytometric analysis highlighted the temporal differences between lung and peripheral blood with respect to increases in these immune cell populations (fig. S3).

Multicolor immunofluorescence microscopy confirmed the spread of virus with increasing time after infection (Fig. 1, F to H, and fig. S4A). Virus-containing AT2 cells exhibited diminished prosurfactant protein C (pSPC) expression that matched loss of surfactant protein C (*Sftpc*) gene expression by 6 dpi (fig. S4B). This correlated with the predicted decrease in AT2s by cell deconvolution at 4 dpi, suggesting that tissue damage observed as a loss of pSPC presents from a very early phase in this PR8 infection model (Fig. 1F and fig. S4C). Neutrophils and monocytes accumulated in the lungs and induced bronchiolitis at 4 dpi and persisted to 7 dpi (Fig. 1G). At 7 dpi, pSPC expression was almost completely lost, indicating severe pathology (Fig. 1H). Conventional histologic examination using hematoxylin and eosin staining also confirmed the severe lung pathology with evidence of neutrophil and mononuclear cell infiltration into bronchi(oles) and alveoli (fig. S4, D and E). We concluded that in this fatal PR8 infection model there were distinct phases of virus- and immune cell–associated damage and severe pathology, including data consistent with the emphasis on innate inflammatory processes reported in prior studies (*5*, *6*, *8*, *9*).

[1]Lymphocyte Biology Section, Laboratory of Immune System Biology, National Institute of Allergy and Infectious Diseases, National Institutes of Health, Bethesda, MD, USA. [2]Florida Research and Innovation Center, Cleveland Clinic Lerner Research Institute, Port Saint Lucie, FL, USA. [3]UCL Institute of Ophthalmology, University College London, London, UK. [4]Center for Advanced Tissue Imaging, Laboratory of Immune System Biology, National Institute of Allergy and Infectious Diseases, National Institutes of Health, Bethesda, MD, USA. *Corresponding author. Email: rgermain@niaid.nih.gov (R.N.G.); hiroshi.ichise@nih.gov (H.I.)
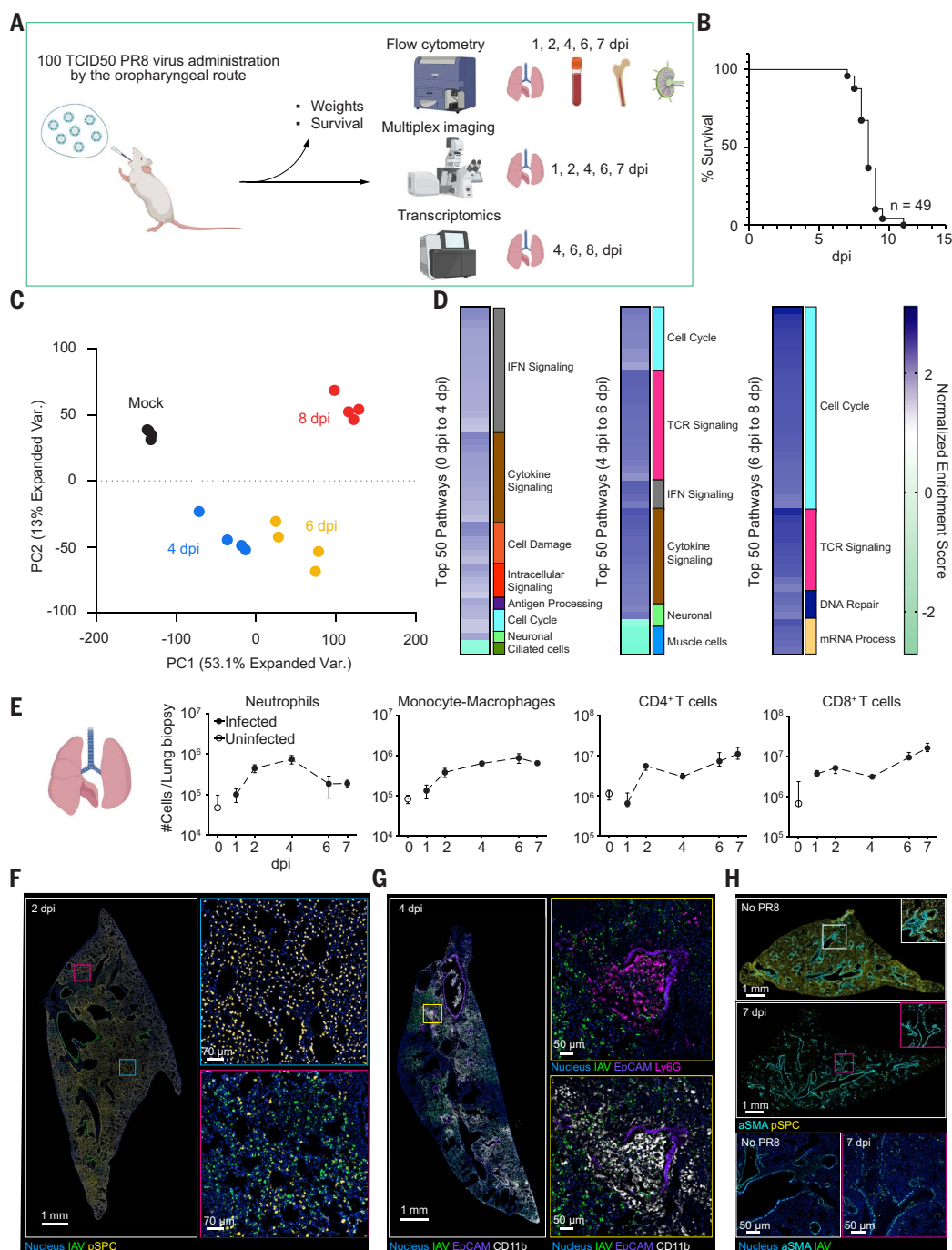
Fig. 1. Characterization of a lethal PR8 infection model. (**A**) Overview of the experimental setup. Mice were infected with 100 TCID$_{50}$ (median tissue culture infectious dose) of PR8 via the oropharyngeal (OPh.) route, and body weight and survival were monitored. Infected animals were euthanized on 1, 2, 4, 6, and 7 dpi, and the lungs, peripheral blood, lung-draining lymph nodes, and bone marrow were collected for flow cytometry and imaging. Lung samples from 4, 6, and 8 dpi were used for RNA-seq. (**B**) Kaplan-Meier plot of survival after PR8 infection. (**C**) Principal components analysis (PCA) of the global transcriptional changes from RNA-seq data at mock (black), 4 dpi (blue), 6 dpi (yellow), and 8 dpi (red) time points. (**D**) Groupings of the top 50 pathways based on adjusted P value ranking from differential expression results at each day compared with the previous day. Values presented are the normalized enrichment score (NES) and are clustered into major groups on the basis of the Jaccard index similarity between the genes in each pathway. (**E**) Flow cytometric analysis of the absolute number of different immune cell types in the lung samples. Each dot represents the mean, and error bars represent the standard error of the mean (SEM). (**F** to **H**) Fluorescence microscopy imaging of lungs from control and infected animals at 2, 4, and 7 dpi. Colored squares show the region magnified in the panels to the right. IAV, influenza A virus nucleoprotein; pSPC, prosurfactant protein C; EpCAM, epithelial cell adhesion molecule; aSMA, alpha-smooth muscle actin. Scale bars: 1 mm on the left and 70 μm on the right images (F); 1 mm on the left and 50 μm on the right images (G); 1 mm on the top two images and 50 μm on the bottom two images (H). Data are representative of at least five independent experiments with at least seven animals in a group, except for (C) to (E); data from one experiment, $n = 4$ mice per group.

Early innate immunomodulation is not sufficient to rescue severe PR8 infection

To examine whether interference with inflammatory damage would ameliorate lethality in this model, we tested >50 regimens that inhibited innate immune cell activity, signaling pathways, cytokines, and alarmins, with early or midcourse dosing of the drugs from 1 to 4 dpi (figs. S5 and S6 and table S2). With the exception of treatments targeting neutrophils [zileuton and anti-Ly6G (lymphocyte antigen 6G) depleting antibody], whose effects were very modest, none of these regimens resulted in survival of infected animals (fig. S5, B and C). In contrast, early high-dose treatment with the antiviral neuraminidase inhibitor Tamiflu led to complete survival of the treated cohort (fig. S5D). Thus, we concluded that interference with innate immune function is not sufficient to robustly prevent death from infection even when used relatively early after infection or in combination with drugs having distinct targets.

Lethality-associated viral and immune damage occurs at very early stages

Our results prompted us to investigate when and how damage leading to death became apparently irreversible in our model. In influenza infections, there are two major pathways of tissue damage: immune-mediated tissue damage and direct cytopathic effect of the virus (19). To unravel the contributions of these two pathologic processes, we titrated anti-Ly6G antibody and Tamiflu to enable interference with innate immune-mediated tissue damage (5) and virus-mediated tissue damage, respectively.

Titration of anti-Ly6G antibody showed a dose-dependent effect on host survival, although at higher concentrations of antibody than previously reported (fig. S7, A and B) (5). This form of antibody treatment had an incomplete effect on lung infiltration by neutrophils seen on day 3 dpi (fig. S7C), a time when these cells filled some of the airways (movie S1). Compared with phosphate-buffered saline (PBS) treatment, neutrophil attenuation improved host survival only when administered on 1 dpi (Fig. 2, A and B). In line with the drop of total neutrophils in the lung at 3 dpi (fig. S6C), animals treated with anti-Ly6G at 1 dpi showed less bronchiole clogging (Fig. 2, C and D). A combination of anti-Ly6G and anti-rat immunoglobulin κ light chain (20) resulted in a five times greater depletion of neutrophils in lung tissue, and a preinfection depletion of neutrophils with an anti-Ly6G treatment at −1 dpi, did not increase survival (fig. S7, B and C). The failure of predepletion to improve survival was consistent with evidence that neutrophils not only cause tissue damage contributing to lethality but also contribute to constraining viral pathology. Moreover, anti-Ly6G treatment could also have led to depletion of Ly6G+ macrophages that can enhance tissue repair (21), which may also have limited the utility of treatments involving anti-Ly6G. We conclude that tissue damage caused by neutrophils becomes irreversible at relatively early stages of infection.

To determine when lethality-associated viral-mediated damage occurred, we conducted a time course study with Tamiflu (Fig. 2E). Starting treatment at 2 dpi, when the viral RNA reached a peak, followed by daily administration of the drug, resulted in uniform survival (Fig. 2F). However, treatment starting on 3 dpi resulted in only partial animal rescue, suggesting that existing viral-mediated damage and associated immune effects could not be overcome by inhibition of further viral spread. Notably, animals treated with Tamiflu starting at 2 dpi had lung damage that was visible at 50 dpi, with scarring, loss of AT2 cells and/or cell function, and myeloid cell infiltration as dominant features (Fig. 2, G and H). Thus, lethality-associated tissue damage mediated by virus and the innate immune system were established early during infection, before animals started losing body weight.

Limiting immune or viral damage enhances tissue repair responses

We addressed what biological processes were promoted when we limited viral- or immune-mediated damage early during infection. Epithelial cell proliferation can be an indication of tissue repair (22), and bulk RNA-seq data from the lungs of infected but untreated animals showed evidence of a burst of proliferation at 8 dpi (Fig. 1C). Infected animals treated with PBS only showed a moderate increase in Ki67+ bronchial epithelial cells at 6 dpi compared with uninfected controls (Fig. 3A). However, animals treated with Tamiflu on 2 dpi showed an increase in Ki67 in the airway epithelium when compared with PBS-treated animals at 6 dpi (Fig. 3, A and B). When animals were treated with anti-Ly6G antibody to limit neutrophil influx, there was an increase in Ly6C+Arginase-1+ macrophages, known to be inducers of tissue repair (23), in the lung at 6 dpi compared with PBS-treated animals (Fig. 3C and fig. S7, D and E) in addition to reduced bronchiolitis (Fig. 2, C and D). These macrophages were found in proximity to an increased number of Ki67+ airway epithelial cells (Fig. 3, C and D, and fig. S7D). We concluded that ongoing viral propagation and immune responses limited tissue repair. In the context of infection that initiates severe viral and innate immune damage during early stages, unaided tissue repair may not be able to maintain an adequate level of pulmonary function.

Combination treatments to enhance repair and limit both viral and late adaptive immune damage improve host survival

The differentiation and proliferation of AT2 cells are important for repairing the lung epithelial layer, as AT2 cells act as a reservoir of stem cells for replacement of alveolar type 1 (AT1) cells in the presence of insults causing pulmonary epithelial damage (24). Patients dying of COVID-19 showed evidence of stressed AT2 cells, consistent with ineffective tissue repair (25). Type I IFN signaling pathways suppress proliferation and induce the death of AT2 cells during recovery from influenza infection (26). The activity of CD8+ T cells, part of the adaptive immune response, may override ongoing tissue repair by killing infected AT1 and AT2 cells (24, 27–29), with loss of AT1 contributing to decreased lung gas exchange capacity.

In our model of lethal influenza, we observed early and sustained expression of many type I IFN–responsive genes (fig. S8A). We also found evidence of T cell–associated signaling and accumulation of CD8+ T cells in the lung beginning at 6 dpi that was correlated with further loss of surfactant proteins and the corresponding gene transcripts (Fig. 1, D and E, and fig. S4, B and C). We hypothesized that to rescue animals that had already passed the early "tipping-point" following lethal infection, tissue repair would have to be enhanced to overcome the existing damage or pathology mediated by adaptive immune responses that arise later during infection would need to be limited, all while restricting viral replication. This led us to consider a combination of late inhibition of viral spread together with blocking of type I IFN signaling or depletion of CD8+ T cells to rebalance tissue damage and repair and salvage animals.

We altered the timing and dose of Tamiflu to determine the conditions when the drug, when administered alone, no longer induced robust host survival. A clinically relevant dose (20 mg/kg) had a moderate effect even when used beginning on 2 dpi, with treatments starting on 4 and 5 dpi showing comparable results, with around 40% survival and a delayed time to death (fig. S8B). On the basis of these data, we proceeded with a treatment starting with 4 dpi at 20 mg/kg, a protocol that mimics a clinically relevant scenario in which patients seek treatment several days to a week after symptoms begin.

We treated infected animals with either anti–interferon-α/β receptor antibody (αIFNAR) or anti-CD8 antibody (αCD8) concurrently with Tamiflu, Tamiflu alone, or PBS (Fig. 4A) and verified the efficacy of the drug (fig. S8, C and D). Both combination treatments improved the survival rate compared with Tamiflu alone (Fig. 4B). The combination of Tamiflu with anti-IFNAR antibody improved body weight beginning at 12 dpi compared with Tamiflu alone, and this difference was maintained to 14 dpi (fig. S8E). Combining anti-IFNAR and anti-CD8
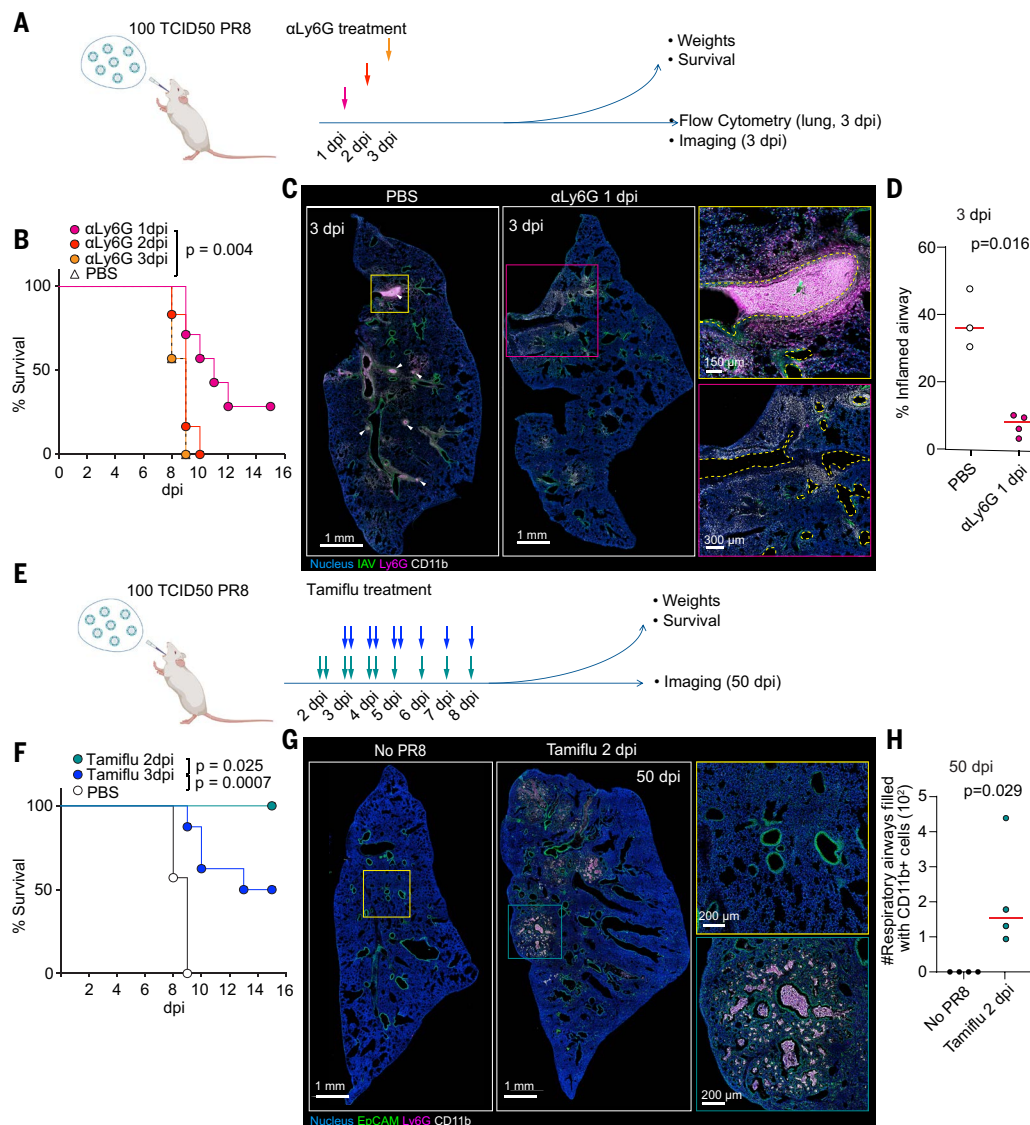
Fig. 2. Irreversible viral and immune damage occur at very early stages of infection. (**A**) Overview of neutrophil depletion experiment. Mice were infected with 100 TCID$_{50}$ of PR8 via the OPh. route, and anti-Ly6G antibody was administered intraperitoneally on either 1, 2, or 3 dpi. Weight and survival were monitored. (**B**) Kaplan-Meier curve of PR8-infected mice treated with anti-Ly6G antibody. $n = 10$ mice per group. Log-rank test was used to calculate the P value. (**C**) Representative immunofluorescence images of lungs from PR8-infected mice treated with anti-Ly6G antibody on 1 dpi. The lungs were harvested on 3 dpi. Magnified views of highlighted regions are shown on the right. Dashed lines outline bronchi and bronchiole structures. Scale bars: 1 mm (left and middle), 150 μm (top right), and 300 μm (bottom right). (**D**) Quantification of airways infiltrated with neutrophils as shown in (C). P value was calculated from a two-tailed Welch's t test. (**E**) Overview of the oseltamivir (Tamiflu) treatment experiment. Mice were infected as shown in (A), and Tamiflu was administered intraperitoneally starting on either 2 or 3 dpi. Two doses per day were administered for the first three consecutive days, with a single dose on the fourth and fifth days of administration. (**F**) Survival curve of PR8-infected mice treated with Tamiflu. Data are from one cohort with $n = 7$ mice per group. Log-rank test was used to calculate a P value. (**G**) Representative immunofluorescence images of lungs of PR8-infected mice treated with Tamiflu starting on 2 dpi. Magnified views of highlighted regions are shown on the right. The lungs were harvested on 50 dpi from animals surviving after Tamiflu treatment. Scale bars: 1 mm (left and middle) and 200 μm (top and bottom right). (**H**) Quantification of myeloid infiltration in the alveoli shown in (G). P value was calculated from a two-tailed Mann-Whitney U test. In (D) and (H), each dot represents an individual animal, and the red bars represent the median. Data are representative of two independent experiments unless otherwise specified.

antibodies with Tamiflu did not show a synergistic effect but rather a worsened outcome (Fig. 4B). This result indicates that either type I IFN signaling or a CD8$^+$ T cell response is necessary for host defense, even in animals treated with Tamiflu. Treatment with anti-IFNAR or anti-CD8 antibodies alone did not have a survival benefit, highlighting the necessity of limiting ongoing viral-mediated damage. To examine the generalizability of the findings beyond male B6 mice, we used mice of different sex and genetic backgrounds. Combining anti-IFNAR or

anti-CD8 antibodies with Tamiflu was effective in both B6 and Balb/c female mice but less so in Balb/c male mice (fig. S8, F to H). The latter results fit with the evidence that males are more susceptible to severe COVID-19 and show delayed CD8$^+$ T cell responses (*30*, *31*).

To gain insights into the basis for the prosurvival effects of Tamiflu plus anti-IFNAR or Tamiflu plus anti-CD8, we carried out bulk RNA-seq on whole lung tissues (Fig. 5A). At 6 dpi, lung tissues had similar transcriptional profiles, but by 8 dpi, the Tamiflu plus anti-IFNAR
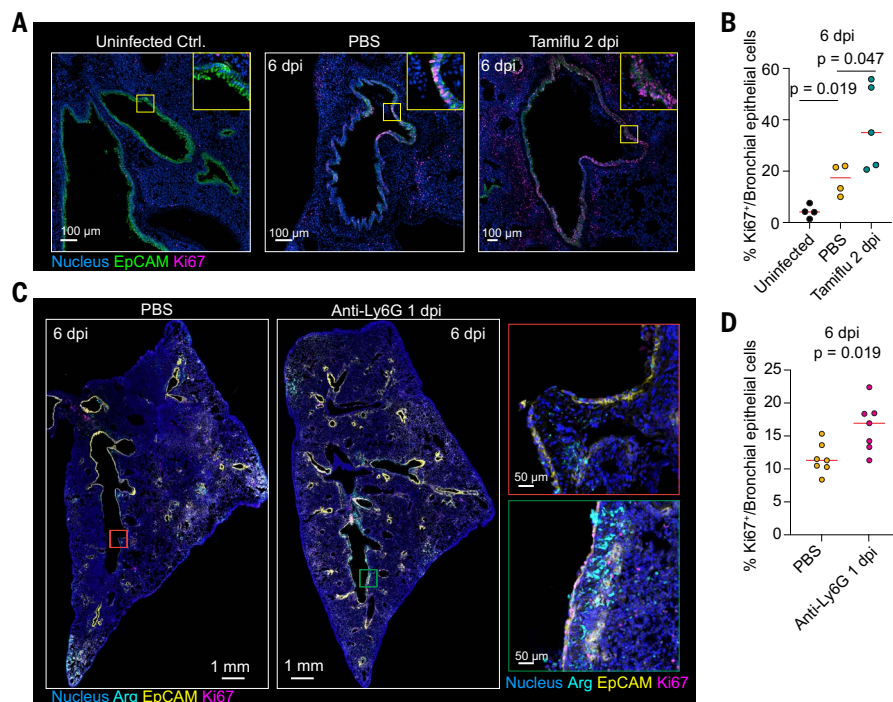
Fig. 3. Limiting immune- or viral-mediated damage changes tissue repair responses. (**A**) Representative immunofluorescence images of lungs of PR8-infected mice treated with Tamiflu starting on 2 dpi. The lungs were harvested on 6 dpi. Scale bar: 100 μm. (**B**) Quantification of Ki67$^+$EpCAM^{high} bronchial epithelial cells as shown in (A). P values were calculated from a two-tailed Welch's t test with multiple comparison correction. (**C**) Representative immunofluorescence images of lungs of PR8-infected mice treated with anti-Ly6G antibody on 1 dpi. The lungs were harvested on 6 dpi. Magnified views of highlighted regions are shown on the right. Arg, arginase 1. Scale bars: 1 mm (left and middle) and 50 μm (top and bottom right). (**D**) Quantification of Ki67$^+$EpCAM^{high} bronchial epithelial cells after indicated treatments as shown in (C). P values were calculated by a two-tailed Welch's t test. In (B) and (D), each dot represents an individual animal, and the red bars represent the median. Data are representative of two independent experiments with n = 4 to 7 mice per group.

samples were distinctive and differed in gene expression associated with cell proliferation, DNA repair, and cilia formation (Fig. 4, C and D, and fig. S9, A to C).

Blocking type I interferon signaling promotes early progenitor cell accumulation and enhanced epithelial repair

In comparison to infected PBS-treated animals at 8 dpi, lung tissues from mice treated with both Tamiflu and anti-IFNAR had evidence of down-regulated type I IFN signaling, but keratinization was enriched (Fig. 5A). Three keratin (KRT)–related genes (*Krt14*, *Trp63*, and *Krt5*) were only expressed in Tamiflu plus anti-IFNAR samples and not in tissues from mice treated with PBS (Fig. 5B). These genes are markers of differentiating basal epithelial cells whose expression increases in the lung after injury, and KRT14$^+$p63$^+$KRT5$^+$ cells can act as progenitors to damaged epithelial layers (*32*). In addition, the data from the Tamiflu plus anti-IFNAR condition predicted enrichment of mesenchymal-like cells at 8 dpi compared with uninfected controls (fig. S10A). These cells play an important role in promoting proliferation of AT2 cells and regenerating the epithelial layers of the lung (*33*, *34*). By 12 dpi, the lung tissue from infected mice treated with Tamiflu alone had up-regulated similar gene programs, suggesting a delayed repair response owing to ongoing interferon responses in the lungs. We concluded that anti-IFNAR treatment in combination with Tamiflu induced an earlier and/or enhanced repair program in the lungs that promoted pulmonary function. Indeed, compared with mice treated with Tamiflu alone, at 8 dpi, animals given anti-IFNAR antibody with Tamiflu maintained

bronchial epithelial cells (fig. S10, B and C), consistent with the prorepair basal epithelial cell differentiation gene signature. These data are consistent with pSTAT1 (phospho-signal transducer and activator of transcription 1) staining in immune cells, AT2, AT1, and mesenchymal cells. All populations had higher pSTAT1 compared with uninfected controls, indicating direct IFN responses in these cell types (fig. S10D).

STAT3 signaling in AT2 cells promotes alveolar epithelial regeneration through the brain-derived neurotrophic factor (BDNF)–tropomyosin-related kinase receptor B (TrkB) axis (*33*). The combination of anti-IFNAR antibody with Tamiflu increased the frequency of cells showing phosphorylation of STAT3 as well as the expression of Ki67 in the AT2 population (Fig. 5, C to F). The absolute number of total and proliferating pSTAT3$^+$ AT2 cells was higher in the animals treated with the combination of anti-IFNAR antibody and Tamiflu (fig. S10, E and F). These cellular changes were associated at 14 dpi in the Tamiflu plus anti-IFNAR condition with an improvement in pulmonary function as compared with 8 dpi that was not observed in the Tamiflu-alone condition (Fig. 5G). Thus, inhibition of the type I IFN response promoted early stem-like cell accumulation that can induce repair of the epithelial layers and facilitate proliferation of AT2 cells, countering the effects of immune and virus-mediated damage and maintaining or improving gas exchange capacity.

Inhibition of CD8$^+$ T cell responses limits severe loss of pneumocytes

Compared with infected PBS-treated animals at 8 dpi, lung tissues from mice given Tamiflu plus anti-CD8 had indications of decreased T cell receptor–associated signaling (fig. S11A). In PBS-treated animals, T cell responses were enriched by 6 dpi (Fig. 1D). This was associated with a loss of surfactant gene expression (fig. S4B) and loss of pSPC staining (Fig. 1H) in the whole lungs, suggesting the contribution of CD8$^+$ T cells to a reduction of AT2 cells. When analyzing the expression of surfactant genes from the RNA-seq data across the time course (Fig. 4A), tissues from mice treated with Tamiflu plus anti-CD8 showed a mild decrease in surfactant genes at 6 dpi compared with uninfected controls and no increase in the loss at 8 dpi (fig. S11B). This was accompanied by reduced viral clearance with a high level of viral RNA still present on 12 dpi (fig. S11, C to H). Lungs from animals treated with the combination of anti-CD8 antibody and Tamiflu had more staining for the virus at 8 dpi (fig. S11I), associated with an increased number of pSPC-producing cells that were positive for IAV (Fig. 6, A to D, and fig. S12). Consistent with infected AT2 cells being preserved, the total number of such cells was higher in animals treated with Tamiflu plus anti-CD8 than in animals treated with Tamiflu alone (Fig. 6E). Tamiflu plus anti-CD8–treated animals also had more AT1 cells than animals treated with Tamiflu alone (Fig. 6, F and G) and less apoptosis in this cell population (Fig. 6H). Mice treated with Tamiflu plus anti-CD8 had higher blood oxygen saturation (SpO$_2$) values compared with those treated with Tamiflu alone (Fig. 6I), indicating better gas exchange capacity in the lung. These data suggested that Tamiflu can diminish viral damage despite not entirely preventing continued epithelial cell infection and that CD8$^+$ effector T cells contribute to loss of respiratory function at late times by killing these infected cells.
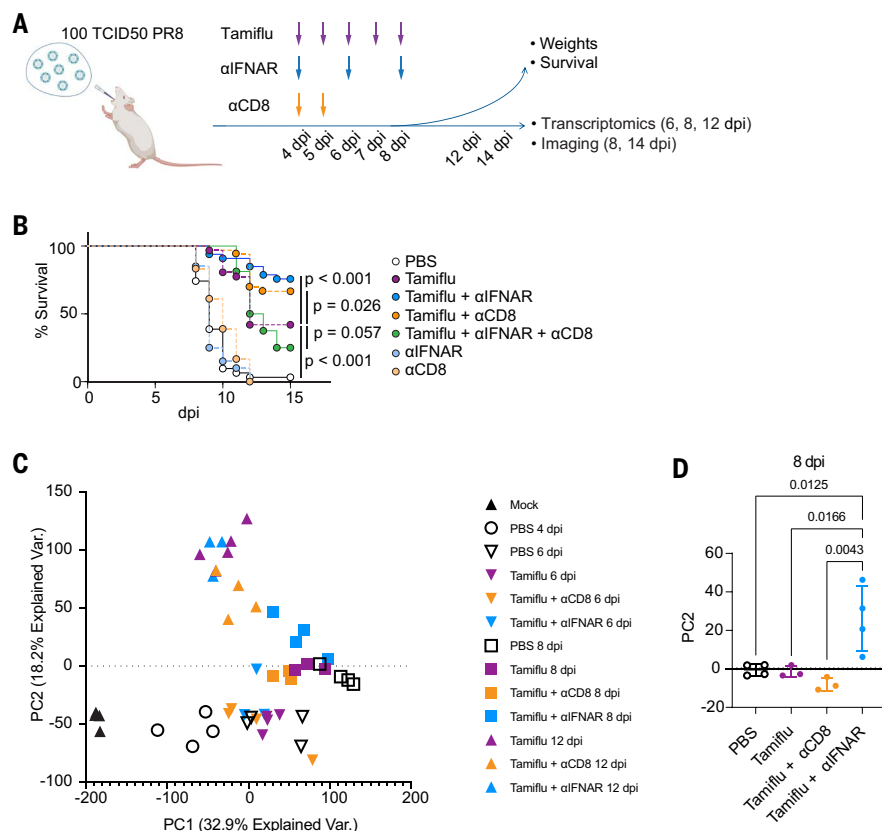
Fig. 4. Combination strategies that target type I IFN signaling or CD8$^+$ T cell response in addition to viral-mediated damage improve host survival. (**A**) Overview of combination treatments to enhance repair and limit both viral and adaptive immune damage. Mice were infected with 100 TCID$_{50}$ of PR8 via the OPh. route, and Tamiflu and/or anti-CD8 antibody and/or anti-IFNAR antibody were administered intraperitoneally at the indicated time points. Weight and survival were monitored. RNA-seq and immunofluorescence imaging were carried out at 4, 6, and 8 dpi and 8 and 14 dpi, respectively. (**B**) Kaplan-Meier plot of infected mice given PBS ($n = 32$), Tamiflu ($n = 31$), Tamiflu plus αIFNAR ($n = 33$), Tamiflu plus αCD8 ($n = 33$), Tamiflu plus αIFNAR plus αCD8 ($n = 16$), αIFNAR ($n = 20$), and αCD8 ($n = 20$). Log-rank test was used to calculate P values. Data are aggregated from two to four independent experiments. (**C**) PCA from RNA-seq of all samples and all conditions, showing the first two principal components. (**D**) Location of samples from 8 dpi along principal component (PC) 2. An ordinary one-way analysis of variance (ANOVA) was used to compare samples to Tamiflu plus αIFNAR. In (C) and (D), each symbol represents an individual animal, and the error bars represent mean $\pm$ SD (standard deviation). Data are from one experiment. $n = 3$ or 4 mice per group.

Discussion

Finding treatment strategies that prevent death when administered late in the course of severe viral pneumonia has proven difficult. Antiviral drugs are the primary choice for hospitalized patients in addition to supportive care, and early treatment with such agents is highly recommended (15). Here, we applied multiple analytical technologies to uncover the factors preventing effective treatment with either anti-inflammatory or antiviral agents when started late in disease. Our findings indicate that the damage arising shortly after disease onset overwhelms the repair capacity of the tissue and passes a tipping point of minimal pulmonary function, with homeostasis being difficult to regain. Thus, we propose that later in viral pneumonias, and possibly also in the case of various forms of ARDS, recovery will be favored if there is a rebalancing of immune- and viral-mediated damage and tissue repair.

Two lines of evidence suggest that type I IFNs might be key to rebalancing damage and repair. First, although type I IFNs are a crucial component of host immunity with antiviral and immune regulatory functions, these cytokines have been recognized to be pathogenic in

pulmonary infectious diseases such as influenza, SARS-CoV, and SARS-CoV2 (13, 35, 36). Previous studies have highlighted that the timing of type I IFN production is critical to the protective versus pathogenic influence of this innate response in SARS-CoV infection and MERS-CoV infection models (18, 37). Early administration (≤ 5 days after hospitalization) of IFN-α2b was associated with reduced mortality of hospitalized patients with COVID-19, whereas late administration was associated with increased mortality (38). Additionally, type I and type III IFNs inhibit AT2 cell proliferation and action as a source of stem cells for repair (26). Given the robust effect of anti-IFNAR treatment in our experiments, it appears that the type III IFNs play a secondary role in our infection model, but additional work is needed to determine whether adding inhibition of the latter would enhance the rescue effect we see (26).

In addition to AT2 cells, cell types such as KRT5$^+$KRT14$^+$p63$^+$ basal cells also serve as sources of regeneration after lung damage (39, 40). Mesenchymal cells provide fibroblast growth factor ligands that act on epithelial stem cells to promote airway regeneration and on AT2 cells to promote alveolar repair (41). Our findings indicate that these cell types accelerate repair upon inhibition of type I IFN signaling. A requirement for effective function of AT2 cells and associated stromal elements supporting epithelial repair is consistent with the observations from patients dying of COVID-19 that revealed stress of the AT2 population as a major signal (25).

The strategy to deplete CD8$^+$ T cells emerged from considering that cytotoxic CD8$^+$ lymphocytes might kill cells that, although infected, may have some remaining function. Robust but late-arising CD8$^+$ T cell responses have been associated with a worse outcome in COVID-19 infection (42). Our data were consistent with depletion of CD8$^+$ T cells promoting enhanced survival, although this was permissive to continued viral replication, which was attenuated by the simultaneous use of Tamiflu.

Our studies showed that different mechanisms accounted for the benefit of these two late treatment regimes, suggesting that there are multiple ways to balance the rate of cell death and tissue preservation to maintain organ function. Thus, it is possible that the other immunomodulatory agents we evaluated in our study might have efficacy in combination with effective antiviral therapy even though single treatment with such drugs show marginal-moderate effects in human trials in COVID-19 (16, 43–47) in combination with high O$_2$ or mechanical ventilation.

Our approach highlights the value of focusing on the temporal evolution of distinct causes of tissue damage in viral ARDS and of the effects of the evolving immune response on repair processes in designing more-effective therapies when early use of potent antivirals has not occurred. Indeed, we propose that our results suggest that the current recommendation against use of Paxlovid and Tamiflu more than 5 days after symptoms begin for COVID-19, or 3 days in the case of influenza, may not maximize use of these drugs, particularly if employed in combination with additional treatments to limit severe disease. These findings provide a rationale for future clinical studies aimed at ameliorating severe influenza when antiviral treatments are no longer effective on their own.
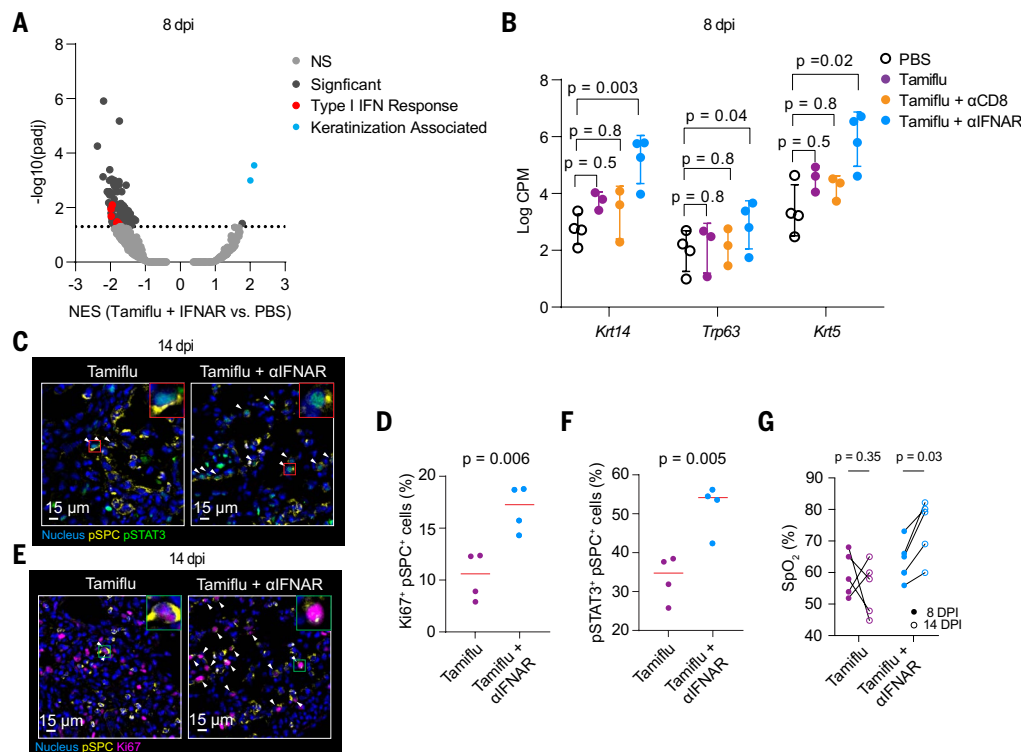
Fig. 5. Combination strategies that target type I IFN signaling in addition to viral-mediated damage enhance early tissue repair. (**A**) Pathway analysis of Tamiflu plus αIFNAR compared with PBS only. The NES score is on the *x* axis, and the −log₁₀(adjusted *P* value) is on the *y* axis. Pathway groupings are colored dots (NS, not significant). (**B**) Differential expression analysis of three genes in each condition compared with PBS. False discovery rate is shown from the edgeR glmLRT (generalized linear model likelihood ratio test). Each dot represents an individual animal, and the error bars represent mean ± SD. (**C** to **F**) Immunofluorescence images and quantification of pSTAT3⁺ [(C) and (D)] or Ki67⁺ [(E) and (F)] AT2 cells in lungs from PR8-infected mice treated with Tamiflu or Tamiflu plus anti-IFNAR antibody starting on 4 dpi. The lungs were harvested on 14 dpi. White arrowheads indicate pSTAT3⁺pSPC⁺ cells in (C) or Ki67⁺pSPC⁺ cells in (E). Scale bars: 15 μm. In (D) and (F), *P* values were calculated from a two-tailed Mann-Whitney *U* test. (**G**) SpO₂ of animals given the indicated treatments after PR8 infection. SpO₂ was measured at 8 and 14 dpi. In (G), two-way ANOVA with Sidak's multiple comparison test was used to calculate *P* values. Each dot represents an individual animal, and in (D) and (F), the red bars represent the median. In (G), the data for individual mice at each time are indicated by the connecting line. Data are representative of two independent experiments, except for (A) and (B), where data are from one experiment. *n* = 3 or 4 mice per group.

Materials and methods

Animals, infections, and tissue collection

Eight- to twelve-week-old male C57BL/6 mice were infected with different doses of H1N1 influenza A viruses via the oropharyngeal route under isoflurane anesthesia. For studies to address generalizability, C57BL/6 female mice, Balb/c male mice, and Balb/c female mice were used. Infectious doses were supplied in a volume of 50 μl sterile 0.9% sodium chloride (Farris Laboratories). Drugs or antibodies were injected intraperitoneally in 200 μl volumes. Peripheral blood, the lung-draining lymph nodes, bone marrow, and lungs were harvested at various time points after infection. For histology, left lobes were fixed with BD CytoFix/CytoPerm (BD Biosciences) diluted in PBS solution (1:4) for 1 day at 4°C. After fixation, tissues were washed briefly three times (5 min per wash) in PBS and incubated in 30% sucrose for 1 day at 4°C before embedding in OCT (optimal cutting temperature) compound (Sakura Finetek, Cat. #4583).

All mice were maintained in specific pathogen–free conditions at an Association for Assessment and Accreditation of Laboratory Animal Care accredited animal facility at the National Institute of Allergy and Infectious Diseases (NIAID). Animals are housed in sterile individually ventilated cages on Allentown NexGen racks. Cages are supplied with sterile LabDiet 5V0T - Verified 75 IF/Auto EXT MOD or LabDiet 5V0G

Select Mouse 50 IF/9F Auto rodent diets (Animal Specialties and Provisions), acidified water in sterile bottles, and sterile bedding with fewer than five mice per cage, 22.2° ± 1.6°C, 30 to 70% humidity, and 14 hours light–10 hours dark cycle. Euthanasia was performed with prolonged exposure of CO₂. All procedures were approved by the NIAID Animal Care and Use Committee (NIH) under ASP LISB-4E and follow the Public Health Service Policy and the Guide for the Care and Use of Laboratory Animals.

Virus

All studies used influenza H1N1 A/PR/8/34 (*48*, *49*) seeds (a kind gift from J. R. Bennink, NIAID, NIH) propagated in EX-CELL MDCK Serum-Free Medium for MDCK Cells (Millipore Sigma, Cat. #14581C-1000ML).

Experimental design for drug treatment after PR8 infection

For screening purposes aimed at reducing animal usage and allowing experiments initially conducted during early COVID pandemic research restrictions to proceed, single experiments were performed for each regimen to determine the efficacy according to power calculations in which we assumed 100% fatalities in the untreated group, and with time to death between 6 and 10 dpi, with most occurring at day 7, we would need about three survivors (effect of 0.7) for a significant difference with an alpha of 0.05. This allowed us to run the studies with fewer animals (10 per group) while still expecting some benefit from treatments without expecting very high survival rates. This strategy used dosing regimens derived from prior studies showing that the agents achieved their expected in vivo effects when used in the manner we employed. These expected effects were validated for several of the agents, such as anti–IL-6R and anti–IL-6 (IL, interleukin), whose use led to increased circulating IL-6 and vice versa. In addition, a few of the treatments were repeated without change in dosing, with identical results. Per our animal study protocol guidelines, animals were monitored by facility veterinarians daily and euthanized when their weight decreased by 30%. All drugs and the regimens used in this study are listed in tables S1 and S2.

Oxygen saturation measurement

SpO₂ level was measured with a pulse oximeter (Kent Scientific Corporation, Cat. # MSTAT-JR) according to the manufacturer's guide.

Immunostaining

Frozen lung tissues were cut at 30 μm on a CM3050S cryostat (Leica) and adhered to Superfrost Plus slides (VWR, Cat. # 48311-703) coated with 15 μl of chrome alum-gelatin adhesive (Newcomer Supply, Cat. #1033A). Frozen sections were washed with PBS and then made permeable and blocked in PBS containing 0.3% Triton X-100 (Sigma, Cat. #
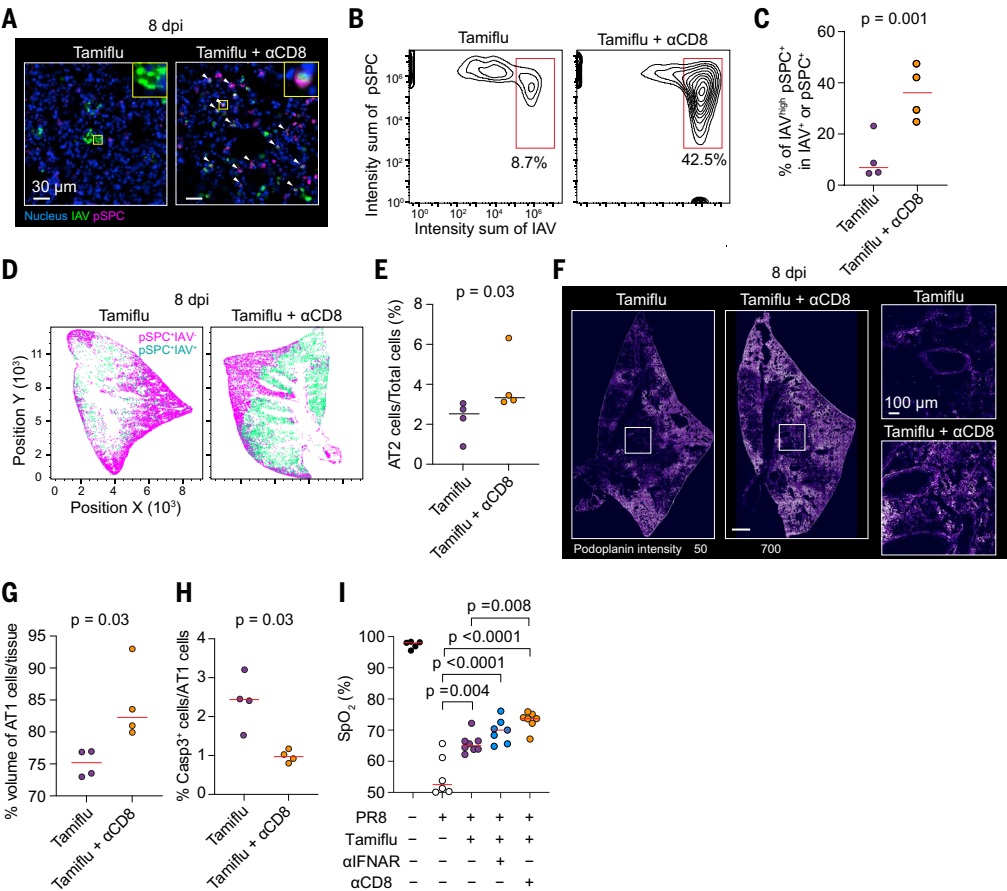
Fig. 6. Combination strategies that target CD8$^+$ T cells in addition to viral-mediated damage prevent loss of pneumocytes. (**A**) Immunofluorescence images of lungs from PR8-infected mice treated with Tamiflu or Tamiflu plus anti-CD8 antibody starting on 4 dpi. The lungs were harvested on 8 dpi. Low magnified views are shown in fig. S11. White arrowheads indicate IAV$^+$pSPC$^+$ cells. Scale bars: 30 μm. (**B** and **C**) Contour plots of AT2 population by histocytometry (B) and the quantification (C). P value was calculated from a two-tailed Welch's t test. (**D**) Histocytometric visualization of pSPC$^+$ IAV$^-$ and pSPC$^+$IAV$^+$ populations. (**E**) Quantification (percentage) of AT2 cells. P value was calculated from a two-tailed Mann-Whitney U test. (**F**) Representative podoplanin staining of lungs from PR8-infected mice treated with Tamiflu or Tamiflu plus anti-CD8 antibody starting on 4 dpi. The lungs were harvested on 8 dpi. Magnified views of highlighted regions are shown on the right. (**G**) Quantification of podoplanin$^+$ region from z-stack immunofluorescence images. (**H**) Quantification of cleaved caspase-3$^+$ AT1 cells from z-stack immunofluorescence images. P values were calculated from a two-tailed Mann-Whitney U test for (G) and (H). (**I**) SpO$_2$ of animals with the indicated treatments after PR8 infection. SpO$_2$ was measured at 8 dpi. P values were calculated from a Tukey's multiple comparison test. Each dot represents an individual animal, and the red bars represent the median. Data are representative of at least two independent experiments. n = 4 to 7 mice per group.

T8787-100ML) and 1% bovine serum albumin (Sigma-Aldrich, Cat. # 10735086001), and 1% mouse Fc block (BD Bioscience, Cat. #553142) followed by staining with antibodies diluted in blocking buffer. The antibodies used in this study are listed in table S3. After staining, slides were mounted with Fluormount G (Southern Biotech, Cat. #0100-01) and examined on a Leica Thunder Imager or TCS SP8 confocal microscope.

Iterative bleaching extends multiplexity (IBEX)

Iterative staining was performed in the principle of the IBEX protocol (*50*, *51*). Briefly, followed by the procedure of immunostaining above, fluorophore inactivation was performed with 1 mg/ml of lithium borohydride for 15 min to inactivate all fluorophores except for Hoechst after image acquisition. Samples were further stained with the antibodies for the second cycle of imaging. Image acquisition was carried out on the same microscope with the same x and y positions. Z plane was adjusted to match the previous round of image with the focus map

function in LAS X Software (Leica Microsystems). Image registration was performed with SimpleITK as previously described (*50*, *51*).

Microscope configuration

Images were acquired using an inverted Leica TCS SP8 X confocal microscope equipped with a 20× objective (NA 0.75), 4 HyD and 1 PMT detectors, a white light laser that produces a continuous spectral output between 470 and 670 nm as well as 405, 685, and 730 nm lasers or Leica THUNDER Imager Tissue equipped with a 20× objective (NA 0.75) (Leica, Cat #11506343), DFC9000 GTC cMOS camera (Leica), LED 8 Fluorescent light source (Leica), CYR71010 filter cube (Leica). Images were captured at 12-bit, with a line average of 3, and 1024-by-1024-pixel format for the confocal imaging or 8-bit depth or 16-bit, 2048-by-2048-pixel format for the Thunder imaging. Tiling images were acquired and merged using the LAS X software.

Image acquisition

Images were acquired using an inverted Leica SP8 confocal microscope equipped with a 20× objective (NA 0.75) (Leica, Cat #11506343) or 40× objective (NA 1.3) (Leica, Cat. #11506429), 4 HyD and 1 PMT detectors, a white light laser that produces a continuous spectral output between 470 and 670 nm as well as 405, 685, and 730 nm lasers or Leica THUNDER Imager Tissue equipped with a 20× objective (NA 0.75), DFC9000 GTC cMOS camera (Leica), LED 8 Fluorescent light source (Leica), CYR71010 filter cube (Leica, Cat. #11525416), and DFT51010 filter cube (Leica, Cat. #11525418). Panels consisted of antibodies conjugated to the following fluorophores

and dyes: Hoechst, eFluor (eF) 450, Alexa Fluor (AF) 488, AF532, PE, AF594, AF647, AF700, AF750, DyeLight 755. Single z plane tiled-images were acquired from whole left lobe sections. To quantify AT1, AT2, and mesenchymal cells and their pSTAT-1 signaling, tiled-z-stack (z-step size: 0.5 μm, 20 slices) images from whole tissue sections were acquired with a Leica SP8 confocal microscope equipped with a 40× objective.

Image processing and analysis

Images were converted to .ims file with Imaris File Converter (Oxford Instruments) and Gaussian filters were applied to all images with Imaris (10.2.0). For cell segmentation and quantification, .ims files were converted to OME-tiff format. The Tissuenet model in Cellpose 2.0 (*52*, *53*), further trained with our dataset, was used to segment cells. Mean intensity of each marker and x, y coordinates were extracted by 3D ImageJ Suite for FIJI (*54*). Extracted values were combined into a single csv file and analyzed by histocytometry as previously described

(*55*). To quantify IAV-NP[high] pSPC^{+} cells, a composite image of IAV-NP and pSPC was created by adding those channels with Imaris channel arithmetic function after subtracting background. After segmentation of IAV-NP[+] and/or pSPC^{+} cells with Imaris surface function based on IAV-NP and pSPC intensity, intensity sum of IAV-NP and pSPC were exported and analyzed by Flowjo software as described previously (*55*). For the quantification of AT1 and AT2 cells in *z*-stack images, we used the Imaris Surface function to segment podoplanin, pSPC, and nucleus signal. The nuclear staining of Ki67, pSTAT1, and pSTAT3 were further quantified on the basis of the threshold function from Imaris.

RNA preparation for RNA-seq

Right inferior lobe was immediately transferred into 1 ml Trizol (Thermo, Cat. #15596018), snap-frozen in liquid nitrogen, and kept at −80°C. RNA extraction was performed by QIAGEN Nucleic Acid Isolation Service (QIAGEN, Germany). RNA integrity number (RIN) was determined with Agilent RNA 6000 Nano Kit (Agilent, Cat. # 5067-1511) for quality check and all samples were above 8.5.

Next-generation sequencing

Sequencing libraries were made from 1 μg total RNA using the TruSeq Stranded mRNA kit, according to the manufacturer's guide (Illumina, San Diego, CA). To obtain reads per sample, 2 μl of each purified library was combined into a single pool, quantified using the Kapa Library Quantification kit (Roche Sequencing Solutions, Pleasanton, CA), diluted to 10 pM, and sequenced as 2×151 bp reads on the MiSeq instrument using the Nano kit, V2 (Illumina, San Diega, CA). A second library pool was created where the volume of each library was calculated on the basis of the read distribution from the MiSeq run to create a normalized pool for deep sequencing. The normalized pool was quantified using the Kapa Library Quantification kit, diluted to 1.8 pM, and sequenced as 2×151 bp paired-end reads on three NextSeq 550 instrument runs using the High Output v2.5, 300 cycle sequencing kit. A total depth of 1.04 billion paired-end reads with an average of 15.3 million paired-end reads per sample was generated.

RNA-seq data processing

After sequencing, samples were aligned to the mouse genome (GRcm39) appended to contain the influenza virus genome (GCF_000865725.1) to account for viral RNA reads. Alignment to the genome was done using STAR v2.7.10 (*56*), and counts were generated using featureCounts in the SubRead package v2.0.4 (*57*). The count tables were read into R v4.2.1. Data normalization and differential expression analysis were performed using edgeR v3.40.2 (*58*). Pathway analysis was performed using the fgsea package v1.24.0 (*59*) and the c2cp gene set from the MSigDB (*60*). Pathways were clustered into groups using a Euclidean distance metric on the Jaccard index of similarity calculation between genes included in the pathway list. Cell type deconvolution from RNA-seq data was performed using the MuSIC package v1.0.0 (*61*) in R and using the naïve lung single cell data form (*62*) as a background. Results were exported to GraphPad/Prism v10.1.1 for display only.

Serum cytokine measurement

Blood obtained by cardiac puncture was placed in Microvette 500 Serum Gel tubes (Sarstedt, 20.1344) and allowed to clot before analysis with the Lunaris Mouse 12-Plex Cytokine Kit (Ayoxxa Biosystems).

Quantitative polymerase chain reaction

Lung samples were collected into tubes containing Trizol (Invitrogen) and manually disassociated in the Trizol followed by processing on direct-zol columns (Zymo Research). RNA concentration was determined on a nanodrop (Thermo Fischer Scientific). cDNA was generated using the SuperScript IV VILO master mix (Invitrogen) and 100 ng/μl of RNA following a program of 25°C for 10 min, 50°C for 10 min, and 85°C for 5 min. cDNA was added to a master mix containing Platinum Quantitative PCR Supermix UDG with ROX (Invitrogen) and the TaqMan (Invitrogen) primer/probe set for influenza A or *Hprt*. Readout was performed in triplicate for each sample using a 15-μl reaction volume in a 384-well plate on the Quant Studio 6 (Thermo Fischer). The viral cycle threshold values were normalized against *Hprt* using the $\Delta\Delta$ method, and the change compared to the average of the controls was calculated.

Flow cytometry

For the lungs, the right cranial lobes were used for all experiments. Harvested lungs were chopped in 2 ml of a mixture of liberase thermolysin medium (TM; 100 μg/ml) (Sigma, Cat. #5401127001) and DNaseI (100 μg/ml) (Roche, Ct. #04716728001) in RPMI-1640 (Thermo Fisher Scientific, Cat. #11875093) and transferred to gentleMACS C Tubes (Miltenyi Biotech, Cat. #130-093-237). Samples were homogenized by two cycles of mechanical dissociation with a gentleMACS Dissociator (Miltenyi Biotech, Cat. #130-093-235) and incubated at 37°C for 30 min for enzymatic digestion in between. Single-cell suspensions were obtained by adding EDTA at a final concentration of 20 mM to stop the enzymatic reaction and passing through a 70 μm nylon mesh. Cells were washed in PBS with 2% fetal bovine serum, 5 mM EDTA (hereafter FACS buffer) twice. The lung-draining lymph nodes were harvested and digested in 500 μl of RPMI with liberase TM (200 μg/ml) at 37°C for 30 min. Single-cell suspensions were obtained by adding EDTA at a final concentration of 20 mM to stop the enzymatic reaction and passing through a 70 μm nylon mesh. Cells were washed in FACS buffer twice. Bone marrow cells were flushed from the femora and tibiae. Suspensions were passed through a 70 μm nylon mesh. Peripheral blood was collected from the inferior vena cava. BD Pharm Lyse Lysing Buffer (BD Biosciences, Cat. #555899) was used to lyse red blood cells. Cells in FACS buffer were blocked with anti-CD16/CD32 (BioLegend, Cat. #101302) and then were incubated with fluorochrome-conjugated antibodies with LIVE/DEAD fixable dead cell stain dye (Thermo Fisher Scientific, Cat. # 423108). Staining and washing were performed at 4°C. CountBright Absolute Counting Beads (Thermo Fisher Scientific, Cat. # C36950) were added into cell suspension before analysis. Cells were analyzed on an LSR Fortessa flow cytometer (BD Biosciences), and data were analyzed with FlowJo software (BD).

Tissue clearing

Volumetric imaging with optically cleared samples were performed as described previously with slight modification (*63*). Briefly, frozen lung samples were sectioned at 500 μm on a CM3050S cryostat. The samples were hydrated and washed with PBS to remove OCT in a 24-well plate. Samples were incubated for at least 12 hours in BD Perm/Wash Buffer (BD Bioscience) containing 1% mouse Fc block (BD Bioscience, Cat. #553142) and stained with titrated antibodies in BD Perm/Wash Buffer (BD Bioscience, Cat. #554723) containing 1% Fc block for 24 hours at room temperature on a shaker. Stained samples were washed with BD Perm/Wash Buffer three times for at least 20 min at room temperature on a shaker. Samples were transferred on a slide with two silicon isolators (Grace BioLabs, Cat. #664407) and treated with 200 μl of Ce3D medium [1.82 g Histodenz (Millipore Sigma, Cat. #D2158-100G, 0.1% triton, and 0.5% thioglycerol (Millipore Sigma, Cat. #M1753) per 1 ml 40% *N*-methylacetamide (Millipore Sigma, Cat. #M26305–500G) in PBS] inside a chemical fume hood and sealed with a cover slip (Electron Microscopy Sciences, Cat. #63766-01) and incubated at room temperature on a shaker overnight. After removing the old Ce3D, cleared samples were mounted with 40 μl of new Ce3D and sealed with a coverslip with two SecureSeal Imaging Spacers (Grace Bio-Labs, Cat. #654002).

Quantification and statistical analysis

Statistical tests performed for a given analysis are denoted in the figure legends. For this manuscript, $P < 0.05$ was considered as a significance threshold. All statistical tests were performed in R or GraphPad/Prism v10.

REFERENCES AND NOTES

1. World Health Organization, Influenza (seasonal); https://www.who.int/news-room/fact-sheets/detail/influenza-(seasonal).
2. D. M. Morens, J. K. Taubenberger, A. S. Fauci, The persistent legacy of the 1918 influenza virus. *N. Engl. J. Med.* **361**, 225–229 (2009). doi: 10.1056/NEJMp0904819; pmid: 19564629
3. N. P. Johnson, J. Mueller, Updating the accounts: Global mortality of the 1918-1920 "Spanish" influenza pandemic. *Bull. Hist. Med.* **76**, 105–115 (2002). doi: 10.1353/bhm.2002.0022; pmid: 11875246
4. J. K. Taubenberger, D. M. Morens, The pathology of influenza virus infections. *Annu. Rev. Pathol.* **3**, 499–522 (2008). doi: 10.1146/annurev.pathmechdis.3.121806.154316; pmid: 18039138
5. M. Brandes, F. Klauschen, S. Kuchen, R. N. Germain, A systems analysis identifies a feedforward inflammatory circuit leading to lethal influenza infection. *Cell* **154**, 197–212 (2013). doi: 10.1016/j.cell.2013.06.013; pmid: 23827683
6. S. Davidson, S. Crotta, T. M. McCabe, A. Wack, Pathogenic potential of interferon αβ in acute influenza infection. *Nat. Commun.* **5**, 3864 (2014). doi: 10.1038/ncomms4864; pmid: 24844667
7. J. R. Teijaro et al., Endothelial cells are central orchestrators of cytokine amplification during influenza virus infection. *Cell* **146**, 980–991 (2011). doi: 10.1016/j.cell.2011.08.015; pmid: 21925319
8. K. L. Lin, Y. Suzuki, H. Nakano, E. Ramsburg, M. D. Gunn, CCR2+ monocyte-derived dendritic cells and exudate macrophages produce influenza-induced pulmonary immune pathology and mortality. *J. Immunol.* **180**, 2562–2572 (2008). doi: 10.4049/jimmunol.180.4.2562; pmid: 18250467
9. T. Narasaraju et al., Excessive neutrophils and neutrophil extracellular traps contribute to acute lung injury of influenza pneumonitis. *Am. J. Pathol.* **179**, 199–210 (2011). doi: 10.1016/j.ajpath.2011.03.013; pmid: 21703402
10. A. L. Totura, R. S. Baric, SARS coronavirus pathogenesis: Host innate immune responses and viral antagonism of interferon. *Curr. Opin. Virol.* **2**, 264–275 (2012). doi: 10.1016/j.coviro.2012.04.004; pmid: 22572391
11. Y. Liang et al., Highlight of immune pathogenic response and hematopathologic effect in SARS-CoV, MERS-CoV, and SARS-Cov-2 infection. *Front. Immunol.* **11**, 1022 (2020). doi: 10.3389/fimmu.2020.01022; pmid: 32574260
12. S. A. Lowery, A. Sariol, S. Perlman, Innate immune and inflammatory responses to SARS-CoV-2: Implications for COVID-19. *Cell Host Microbe* **29**, 1052–1062 (2021). doi: 10.1016/j.chom.2021.05.004; pmid: 34022154
13. R. Channappanavar, S. Perlman, Pathogenic human coronavirus infections: Causes and consequences of cytokine storm and immunopathology. *Semin. Immunopathol.* **39**, 529–539 (2017). doi: 10.1007/s00281-017-0629-x; pmid: 28466096
14. I. Ramos, A. Fernandez-Sesma, Modulating the innate immune response to influenza A virus: Potential therapeutic use of anti-inflammatory drugs. *Front. Immunol.* **6**, 361 (2015). doi: 10.3389/fimmu.2015.00361; pmid: 26257731
15. Centers for Disease Control and Prevention, Influenza Antiviral Medications: Summary for Clinicians; https://www.cdc.gov/flu/hcp/antivirals/summary-clinicians.html.
16. RECOVERY Collaborative Group, Dexamethasone in hospitalized patients with Covid-19. *N. Engl. J. Med.* **384**, 693–704 (2021). doi: 10.1056/NEJMoa2021436; pmid: 32678530
17. P. Mathur, S. Kottilil, Immunomodulatory therapies for COVID-19. *Front. Med. (Lausanne)* **9**, 921452 (2022). doi: 10.3389/fmed.2022.921452; pmid: 35991665
18. R. Channappanavar et al., Dysregulated type I interferon and inflammatory monocyte-macrophage responses cause lethal pneumonia in SARS-CoV-infected mice. *Cell Host Microbe* **19**, 181–193 (2016). doi: 10.1016/j.chom.2016.01.007; pmid: 26867177
19. S. Herold, C. Becker, K. M. Ridge, G. R. S. Budinger, Influenza virus-induced lung injury: Pathogenesis and implications for treatment. *Eur. Respir. J.* **45**, 1463–1478 (2015). doi: 10.1183/09031936.00186214; pmid: 25792631
20. G. Boivin et al., Durable and controlled depletion of neutrophils in mice. *Nat. Commun.* **11**, 2762 (2020). doi: 10.1038/s41467-020-16596-9; pmid: 32488020
21. C. Ruscitti et al., Recruited atypical Ly6G+ macrophages license alveolar regeneration after lung injury. *Sci. Immunol.* **9**, eado1227 (2024). doi: 10.1126/sciimmunol.ado1227; pmid: 39093958
22. M. F. Beers, E. E. Morrisey, The three R's of lung health and disease: Repair, remodeling, and regeneration. *J. Clin. Invest.* **121**, 2065–2073 (2011). doi: 10.1172/JCI45961; pmid: 21633173
23. L. Campbell, C. R. Saville, P. J. Murray, S. M. Cruickshank, M. J. Hardman, Local arginase 1 activity is required for cutaneous wound healing. *J. Invest. Dermatol.* **133**, 2461–2470 (2013). doi: 10.1038/jid.2013.164; pmid: 23552798
24. C. E. Barkauskas et al., Type 2 alveolar cells are stem cells in adult lung. *J. Clin. Invest.* **123**, 3025–3036 (2013). doi: 10.1172/JCI68782; pmid: 23921127
25. T. M. Delorey et al., COVID-19 tissue atlases reveal SARS-CoV-2 pathology and cellular targets. *Nature* **595**, 107–113 (2021). doi: 10.1038/s41586-021-03570-8; pmid: 33915569
26. J. Major et al., Type I and III interferons disrupt lung epithelial repair during recovery from viral infection. *Science* **369**, 712–717 (2020). doi: 10.1126/science.abc2061; pmid: 32527928
27. I. Y. Adamson, D. H. Bowden, The type 2 cell as progenitor of alveolar epithelial regeneration. A cytodynamic study in mice after exposure to oxygen. *Lab. Invest.* **30**, 35–42 (1974). pmid: 4812806
28. W. J. Zacharias et al., Regeneration of the lung alveolus by an evolutionarily conserved epithelial progenitor. *Nature* **555**, 251–255 (2018). doi: 10.1038/nature25786; pmid: 29489752
29. A. N. Nabhan, D. G. Brownfield, P. B. Harbury, M. A. Krasnow, T. J. Desai, Single-cell Wnt signaling niches maintain stemness of alveolar type 2 cells. *Science* **359**, 1118–1123 (2018). doi: 10.1126/science.aam6603; pmid: 29420258
30. S. A. Kharroubi, M. Diab-El-Harake, Sex-differences in COVID-19 diagnosis, risk factors and disease comorbidities: A large US-based cohort study. *Front. Public Health* **10**, 1029190 (2022). doi: 10.3389/fpubh.2022.1029190; pmid: 36466473
31. T. Takahashi et al., Sex differences in immune responses that underlie COVID-19 disease outcomes. *Nature* **588**, 315–320 (2020). doi: 10.1038/s41586-020-2700-3; pmid: 32864427
32. V. Ievlev et al., Krt14 and Krt15 differentially regulate regenerative properties and differentiation potential of airway basal cells. *JCI Insight* **8**, e162041 (2023). doi: 10.1172/jci.insight.162041; pmid: 36512409
33. A. J. Paris et al., STAT3–BDNF–TrkB signalling promotes alveolar epithelial regeneration after lung injury. *Nat. Cell Biol.* **22**, 1197–1210 (2020). doi: 10.1038/s41556-020-0569-x; pmid: 32989251
34. T. Peng et al., Hedgehog actively maintains adult lung quiescence and regulates repair and regeneration. *Nature* **526**, 578–582 (2015). doi: 10.1038/nature14984; pmid: 26436454
35. F. McNab, K. Mayer-Barber, A. Sher, A. Wack, A. O'Garra, Type I interferons in infectious disease. *Nat. Rev. Immunol.* **15**, 87–103 (2015). doi: 10.1038/nri3787; pmid: 25614319
36. S. Davidson, M. K. Maini, A. Wack, Disease-promoting effects of type I interferons in viral, bacterial, and coinfections. *J. Interferon Cytokine Res.* **35**, 252–264 (2015). doi: 10.1089/jir.2014.0227; pmid: 25714109
37. R. Channappanavar et al., IFN-I response timing relative to virus replication determines MERS coronavirus infection outcomes. *J. Clin. Invest.* **129**, 3625–3639 (2019). doi: 10.1172/JCI126363; pmid: 31355779
38. N. Wang et al., Retrospective multicenter cohort study shows early interferon therapy is associated with favorable clinical responses in COVID-19 Patients. *Cell Host Microbe* **28**, 455–464.e2 (2020). doi: 10.1016/j.chom.2020.07.005; pmid: 32707096
39. A. E. Vaughan et al., Lineage-negative progenitors mobilize to regenerate lung epithelium after major injury. *Nature* **517**, 621–625 (2015). doi: 10.1038/nature14112; pmid: 25533958
40. W. Zuo et al., p63+Krt5+ distal airway stem cells are essential for lung regeneration. *Nature* **517**, 616–620 (2015). doi: 10.1038/nature13903; pmid: 25383540
41. E. El Agha, V. J. Thannickal, The lung mesenchyme in development, regeneration, and fibrosis. *J. Clin. Invest.* **133**, e170498 (2023). doi: 10.1172/JCI170498; pmid: 37463440
42. L. Bergamaschi et al., Longitudinal analysis reveals that delayed bystander CD8+ T cell activation and early immune pathology distinguish severe COVID-19 from mild disease. *Immunity* **54**, 1257–1275.e8 (2021). doi: 10.1016/j.immuni.2021.05.010; pmid: 34051148
43. I. O. Rosas et al., Tocilizumab in hospitalized patients with severe Covid-19 pneumonia. *N. Engl. J. Med.* **384**, 1503–1516 (2021). doi: 10.1056/NEJMoa2028700; pmid: 33631066
44. P. O. Guimarães et al., Tofacitinib in patients hospitalized with Covid-19 Pneumonia. *N. Engl. J. Med.* **385**, 406–415 (2021). doi: 10.1056/NEJMoa2101643; pmid: 34133856
45. Y. Cao et al., Ruxolitinib in treatment of severe coronavirus disease 2019 (COVID-19): A multicenter, single-blind, randomized controlled trial. *J. Allergy Clin. Immunol.* **146**, 137–146.e3 (2020). doi: 10.1016/j.jaci.2020.05.019; pmid: 32470486
46. REMAP-CAP Investigators, Interleukin-6 receptor antagonists in critically ill patients with Covid-19. *N. Engl. J. Med.* **384**, 1491–1502 (2021). doi: 10.1056/NEJMoa2100433; pmid: 33631065
47. J. H. Stone et al., Efficacy of tocilizumab in patients hospitalized with Covid-19. *N. Engl. J. Med.* **383**, 2333–2344 (2020). doi: 10.1056/NEJMoa2028836; pmid: 33085857
48. T. Francis Jr., Transmission of influenza by a filterable virus. *Science* **80**, 457–459 (1934). doi: 10.1126/science.80.2081.457.b; pmid: 17795179
49. T. Francis Jr., T. P. Magill, Immunological studies with the virus of influenza. *J. Exp. Med.* **62**, 505–516 (1935). doi: 10.1084/jem.62.4.505; pmid: 19870430
50. A. J. Radtke et al., IBEX: A versatile multiplex optical imaging approach for deep phenotyping and spatial analysis of cells in complex tissues. *Proc. Natl. Acad. Sci. U.S.A.* **117**, 33455–33465 (2020). doi: 10.1073/pnas.2018488117; pmid: 33376221
51. A. J. Radtke et al., IBEX: An iterative immunolabeling and chemical bleaching method for high-content imaging of diverse tissues. *Nat. Protoc.* **17**, 378–401 (2022). doi: 10.1038/s41596-021-00644-9; pmid: 35022622
52. C. Stringer, T. Wang, M. Michaelos, M. Pachitariu, Cellpose: A generalist algorithm for cellular segmentation. *Nat. Methods* **18**, 100–106 (2021). doi: 10.1038/s41592-020-01018-x; pmid: 33318659
53. M. Pachitariu, C. Stringer, Cellpose 2.0: How to train your own model. *Nat. Methods* **19**, 1634–1641 (2022). doi: 10.1038/s41592-022-01663-4; pmid: 36344832
54. J. Ollion, J. Cochennec, F. Loll, C. Escudé, T. Boudier, TANGO: A generic tool for high-throughput 3D image analysis for studying nuclear organization. *Bioinformatics* **29**, 1840–1841 (2013). doi: 10.1093/bioinformatics/btt276; pmid: 23681123

55. M. Y. Gerner, W. Kastenmuller, I. Ifrim, J. Kabat, R. N. Germain, Histo-cytometry: A method for highly multiplex quantitative tissue imaging analysis applied to dendritic cell subset microanatomy in lymph nodes. *Immunity* **37**, 364–376 (2012). doi: 10.1016/j.immuni.2012.07.011; pmid: 22863836

56. A. Dobin *et al.*, STAR: Ultrafast universal RNA-seq aligner. *Bioinformatics* **29**, 15–21 (2013). doi: 10.1093/bioinformatics/bts635; pmid: 23104886

57. Y. Liao, G. K. Smyth, W. Shi, featureCounts: An efficient general purpose program for assigning sequence reads to genomic features. *Bioinformatics* **30**, 923–930 (2014). doi: 10.1093/bioinformatics/btt656; pmid: 24227677

58. M. D. Robinson, D. J. McCarthy, G. K. Smyth, edgeR: A Bioconductor package for differential expression analysis of digital gene expression data. *Bioinformatics* **26**, 139–140 (2010). doi: 10.1093/bioinformatics/btp616; pmid: 19910308

59. G. Korotkevich *et al.*, Fast gene set enrichment analysis. bioRxiv 060012 [Preprint] (2021). https://doi.org/10.1101/060012.

60. A. Subramanian *et al.*, Gene set enrichment analysis: A knowledge-based approach for interpreting genome-wide expression profiles. *Proc. Natl. Acad. Sci. U.S.A.* **102**, 15545–15550 (2005). doi: 10.1073/pnas.0506580102; pmid: 16199517

61. X. Wang, J. Park, K. Susztak, N. R. Zhang, M. Li, Bulk tissue cell type deconvolution with multi-subject single-cell expression reference. *Nat. Commun.* **10**, 380 (2019). doi: 10.1038/s41467-018-08023-x; pmid: 30670690

62. L. M. Roberts *et al.*, Pulmonary infection induces persistent, pathogen-specific lipidomic changes influencing trained immunity. *iScience* **24**, 103025 (2021). doi: 10.1016/j.isci.2021.103025; pmid: 34522865

63. W. Li, R. N. Germain, M. Y. Gerner, Multiplex, quantitative cellular analysis in large tissue volumes with clearing-enhanced 3D microscopy (C$_e$3D). *Proc. Natl. Acad. Sci. U.S.A.* **114**, E7321–E7330 (2017). pmid: 28808033

SUPPLEMENTARY MATERIALS

science.org/doi/10.1126/science.adr4635
Figs. S1 to S12; Tables S1 to S3; Reference (*64*); MDAR Reproducibility Checklist; Movie S1